JOURNAL OF GEOPHYSICAL RESEARCH, VOL. 113, A02209, doi:10.1029/2007JA012653, 2008

Multiscale/multifluid simulations of flux ropes at the magnetopause within a global magnetospheric model

R. M. Winglee,[1] E. Harnett,[1] A. Stickle,[1] and J. Porter[1]

Received 17 July 2007; revised 14 September 2007; accepted 5 November 2007; published 22 February 2008.

[1] The magnetopause current sheet is known to have a thickness comparable to an ion gyroradius/skin depth where the magnetic and electric field can differ markedly from that assumed in MHD treatments. Multifluid/multiscale simulations are used to provide the first investigation of these processes in a global simulation that includes high-resolution (200 km) gridding around the magnetopause. It is shown that the model is able to capture the quadrupole core magnetic field and the fast (tens of ion cyclotron periods) reconnection seen in idealized studies reconnection for a Harris current sheet. Within a global magnetosphere, multiple X-line reconnection occurs for southward IMF due to localized pinching of the magnetopause current sheet via the convection of the magnetosheath plasma against a three-dimensional magnetopause. Localized flux ropes with a thickness of a few hundred to a few thousand kilometers develop and can expand laterally due to current sheet acceleration of ions that have a gyroradius comparable to the current sheet thickness. These flux ropes are shown to have essentially the same properties as flux transfer events (FTEs), including being quasi-periodic with a curvature greater on the magnetosheath side than on the magnetospheric side, a strong core magnetic field, and a mixture of magnetospheric and magnetosheath plasma. The speeds of the plasma flows associated with flux ropes are also similar to those observed with FTEs. The presence of multiple X-line reconnection is shown to produce the rippling of the magnetopause and gives a nature explanation to the multiple magnetopause encounters that typically occur for slow moving spacecraft. These small-scale processes are shown to have global effects with a reduction of the cross-polar cap by as much as 20% seen between simulations with and without high resolution about the magnetopause.

Citation: Winglee, R. M., E. Harnett, A. Stickle, and J. Porter (2008), Multiscale/multifluid simulations of flux ropes at the magnetopause within a global magnetospheric model, *J. Geophys. Res.*, *113*, A02209, doi:10.1029/2007JA012653.

1. Introduction

[2] The magnetopause is critical to the dynamics of the magnetosphere as it is this region that controls the entry of solar wind mass and energy into magnetopause. Magnetic reconnection is an important part of the entry process. For southward interplanetary magnetic field (IMF) an X-line is thought to occur in the vicinity of the subsolar magnetopause [cf. *Gosling et al.*, 1990, and references therein]. Field lines that have undergone reconnection move rapidly along the magnetopause under tension from the curvature of the field lines. In this region, magnetosheath ions from the solar wind side can convect into the reconnection region if they have sufficiently high velocity and magnetospheric ions (albeit at significantly lower densities) can enter the reconnection region from the other side. The ions that enter the reconnection region are accelerated by the reconnection electric fields leading to the accelerated plasma flows along the magnetopause. Slower moving ions that are unable to enter the reconnection region may still experience acceleration if they are on a recently reconnected field lines as the latter moves rapidly along the magnetopause. For northward IMF the reconnection region moves from the subsolar region to high latitude, but the dynamics is thought to be essentially the same.

[3] One of the outstanding questions for magnetopause dynamics is whether the reconnection for southward IMF occurs through a single time-dependent X-line or through multiple X-line reconnection. The model for a single dayside X-line reconnection originates from the Dungey model of the magnetosphere [*Dungey*, 1963] and is a key feature of present day global MHD models [e.g., *Ogino*, 1986; *Slinker et al.*, 1995]. The multiple X-line model was originally put forward by *Dubinin et al.* [1977] and appears in many local simulation models of thin current sheets [e.g., *Lee and Fu*, 1986; *Fu and Lee*, 1986]. For these simulations, multiple X-line reconnection occurs when the thickness of the current sheet decreases below an inherent scale length that is dependent on the magnitude of the anomalous resistivity assumed in the simulations.

[1]Department of Earth and Space Sciences, University of Washington, Seattle, Washington, USA.

0148-0227/08/2007JA012653$09.00

[4] The issue of whether reconnection occurs via single or multiple X-line reconnection is of fundamental importance to the dynamics of the magnetopause. This issue is at the heart of determining the origin and properties of flux transfer events (FTEs) [*Russell and Elphic*, 1978; *Haerendel et al.*, 1978; see also *Elphic*, 1989]. FTEs are associated with local magnetic intensifications or flux ropes with certain magnetosheath particles being able to transit the structure and enter the magnetosphere, while other particles are reflected and/or accelerated along the magnetopause. Similarly, magnetospheric particles may either be reflected or be able to cross into the magnetosheath [*Gosling et al.*, 1990]. FTEs also appear quasi-periodically with an average period of several minutes and an average duration of less than a minute [*Elphic*, 1989].

[5] FTEs and indeed the thickness of the magnetopause are relatively thin. Estimates for the thickness of the magnetopause derived from multispacecraft missions such as ISEE suggest thicknesses ranging from 200 to 1600 km with the median thickness being about 600–800 km [*Berchem and Russell*, 1982; see also *Paschmann*, 1997, and reference therein]. These thin boundary layers have scale lengths that are comparable to or smaller than an ion gyroradius/ion skin depth, which means that the assumptions used in global MHD modeling are no longer valid. Even thinner electron boundary layers have also been observed by Cluster [*André et al.*, 2004].

[6] *Drake et al.* [1994] have shown that for idealized geometries where the current sheet thickness is of the order of an ion gyroradius/ion skin depth, reconnection does not occur in a smooth MHD manner but rather occurs through filamentation and kinking of the current sheet. *Winglee* [1994], *Biskamp et al.* [1995], *Ma and Bhattacharjee* [1996], *Zhu and Winglee* [1996], *Pritchett et al.* [1996], *Shay et al.* [1998], and *Birn et al.* [2001] have all demonstrated using a variety of different codes (including full particle, hybrid, and multifluid) that the Hall term in the generalized Ohm's law plays an important role in controlling the reconnection rate and overall magnetic structure in collisionless plasmas for thin current sheets of the order of a few ion skin depth.

[7] However, the above idealized simulations can only be considered as local treatments. They neglect key features of a real magnetosphere, including the global transport of mass and energy that can lead to inhomogeneities in the forcing on any extended surface in the magnetosphere, especially the magnetopause and magnetotail. On the other hand, a global model that does not incorporate the actual physics of reconnection or the boundary layers will have difficulty in tying results to in situ observations.

[8] In this paper, multifluid/multiscale simulations are used to examine the dynamics of the magnetopause at high resolution with spatial resolution down to 200 km. At this scale length, we begin to resolve some of the key structures within the magnetopause. This study is a first of its type and provides new understanding of small-scale processes at the magnetopause within the global environment. In section 2 the details of the model are given along with a discussion of relevant scale lengths incorporated within the model. Results for the Global Environment Modeling (GEM) reconnection challenge are given in section 2 for a Harris current sheet and demonstrate that the code is able to reproduce key results from hybrid simulations, including the presence of a quadrupole in-plane magnetic field, and the development of fast reconnection.

[9] With this calibration, the multifluid/multiscale is then applied to the modeling of the magnetosphere with high spatial resolution at the magnetopause. Results from the model (section 3) show the development of multiple magnetic islands and flux ropes similar to previous hybrid simulations. The model goes one step further by showing that the reconnection is quasi-periodic in association with the generation of flux ropes and enhanced plasma density and pressure, in associated with the mixing of ionospheric and solar wind ions, similar to *Gosling et al.* [1990]. These flux ropes also have a period that is similar to that seen in association with flux transfer events. In addition, it is shown that including the curvature of the terrestrial magnetosphere eventually leads to the development of asymmetries both in the dawn and dusk sides. In section 5 we discuss how the simulation results would appear to a spacecraft that slowly traverses the magnetopause. The presence of the localized reconnection and quasi-periodic generation reconnection will cause a spacecraft to have multimagnetopause crossings, despite the fact that solar wind conditions are constant. The model results in terms of plasma flows and magnetic signatures are shown to have many features previously reported in the literature in association with in situ observations but missing from present-day global MHD models. A summary of results is given in section 6.

2. Ion Cyclotron/Ion Skin Depth Effects in Multifluid/Multiscale Model

[10] The first attempts to incorporate Hall effects into a 3-D global model used a perturbation expansion [*Winglee*, 1994] valid for $|V \times B| \gg |J \times B|$/en, that provided a first glimpse of how the topology predicted by MHD would be modified by a small but nonzero Hall correction. The model was then improved to fully incorporate of the Hall and grad P terms and demonstrated and even at course resolution of 0.25 R_E these corrections could produce a core magnetic field that is comparable to that observed in tail flux ropes [*Winglee et al.*, 1998]. With the evolution of the multifluid model, the evolution of different sources of ions could be tracked and this work lead to the first three dimensional identification of the geopause, as well as the relative roles of ionospheric and solar wind plasma in populating the magnetosphere [*Winglee*, 2000] and the importance of ionospheric mass outflows in mass loading of the magnetosphere, the generation of the Harang discontinuity and the cross polar cap potential [*Winglee et al.*, 2002, 2005; *Winglee*, 2004]. Excellent agreement with observations has been obtained for weakly magnetized systems such as Mars and Ganymede [*Harnett and Winglee*, 2003, 2007; *Paty and Winglee*, 2004, 2006]. Heavy ion pickup at Pluto as seen in hybrid codes but not MHD has also been demonstrated within the multifluid approach [*Harnett et al.*, 2005].

[11] The present version of the code includes a full incorporation of ion skin depth effects in the Ohm's law and ion cyclotron terms in the momentum equation [*Winglee et al.*, 2005]. The specifics of the code are as follows. The

dynamics of each plasma component is described by mass, momentum, and pressure equations given by

$$\frac{\partial \rho_\alpha}{\partial t} + \nabla \cdot (\rho_\alpha \boldsymbol{V}_\alpha) = 0 \tag{1}$$

$$\rho_\alpha \frac{dV_\alpha}{dt} = q_\alpha n_\alpha (E + V_\alpha \times B(r)) - \nabla P_\alpha - \left(\frac{GM_E}{R_E^2}\right)\rho_\alpha \vec{r} \tag{2}$$

$$\frac{\partial P_\alpha}{\partial t} = -\gamma \nabla \cdot (P_\alpha \boldsymbol{V}_\alpha) + (\gamma - 1)\boldsymbol{V}_\alpha \cdot \nabla P_\alpha \tag{3}$$

where the subscripts α denotes the ion and electron components that constitute the plasma. In both hybrid codes and the multifluid code one makes the assumption that the electrons are fluids and that they have sufficiently high mobility along the field lines such that they are approximately in steady-state (i.e., d/dt = 0) or in drift motion. This assumption removes high-frequency plasma waves and electron waves but enables the momentum equation for the electrons to be reduced to

$$\boldsymbol{E} + \boldsymbol{V}_e \times \boldsymbol{B} + \frac{\nabla P_e}{en_e} = 0 \tag{4}$$

The electron dynamics are completed by assuming quasi-neutrality and applying the definitions for current and electron pressure. For a single component plasma one obtains

$$N_e = N_i, \quad \boldsymbol{V}_e = \boldsymbol{V}_i - \frac{\boldsymbol{J}}{\mathrm{eN_e}}, \quad \boldsymbol{J} = \frac{1}{\mu_0}\nabla \times \boldsymbol{B} \tag{5}$$

$$\frac{\partial P_e}{\partial t} = -\gamma \nabla \cdot (P_e \boldsymbol{V}_e) + (\gamma - 1)\boldsymbol{V}_e \cdot \nabla P_e \tag{6}$$

In hybrid codes the ions are loaded as an ensemble of superparticles that represent the particle distribution with the prescribed temperature and density. The particle ions are moved by the Lorentz force equation

$$m_n \frac{dv_n}{dt} = q_n(\boldsymbol{E}(\boldsymbol{r}) + v_n \times \boldsymbol{B}(\boldsymbol{r})) \tag{7}$$

where the subscript denotes that nth particle. Bulk properties of the plasma, in particular the ion number density N_i and the average ion velocity V_i, are determined by interpolating the particle equivalent density and velocity onto the nearest grid points and summing over all particles. The electric field is then obtained by substituting the derived quantities $\mathrm{N_i}$ and $\mathrm{V_i}$ in (5) into the Ohm's Law (4), and the magnetic field is updated by using this electric field in the induction equation

$$\frac{\partial \boldsymbol{B}}{\partial t} + \nabla \times \boldsymbol{E} = 0 \tag{8}$$

[12] The advantage of the hybrid code is that by having particle ions one is able to fully address the particle acceleration at ion skin depth/ion cyclotron effects. The disadvantage of hybrid codes is that they have to carry enough particles to represent the particle distribution in both coordinate and velocity space within each cell. For example, suppose that one has 100 particles per cell presenting the peak density of the current sheet. The minimum density change that this code could reasonably resolve is therefore only a few percent below which one would obtain with only a particle or two (or zero) per cell and would not yield an accurate result. While one might be able to estimate the density, one cannot accurately reconstruct a velocity distribution with so few particles, and an integration (i.e., loss of spatial resolution) must be performed to generate reasonable statistics for the bulk velocity and temperature.

[13] The multifluid/multiscale treatment used here is based on the observation that hybrid (and full particle) codes all have to take bulk moments of the particles onto the grid system in order to advance the magnetic and electric fields, which are then used to advance the particles. The multifluid treatment therefore simplifies the process by solving the fluid equations (1)–(3) for the bulk moments for the ions, which still include ion cyclotron effects (as opposed to MHD where the equations are collapse and ion cyclotron terms are neglected). One can show from a wave analysis that equations (1)–(3) incorporate the full spectrum of waves up to the lower hybrid portion of the whistler mode when the electric field is specified by (4) as opposed to the ideal Ohm's law. Because the code tracks fluid elements which are continuous, it can have a larger dynamic range in density and temperature. Additionally, because one is not tracking large numbers of particles, the code can support much larger grid systems.

[14] In the multifluid treatment, we assume three different ion components: (1) solar wind protons, (2) ionospheric protons, and (3) ionospheric O^+ ions. With these multiple components present, (5) is modified to

$$n_e = \sum_i n_i, \quad \boldsymbol{V}_e = \sum_i \frac{n_i}{n_e}\boldsymbol{V}_i - \frac{\boldsymbol{J}}{\mathrm{en_e}}, \quad \boldsymbol{J} = \frac{1}{\mu_0}\nabla \times \boldsymbol{B} \tag{9}$$

Substitution of (9) into (4) yields the modified Ohm's law of

$$\boldsymbol{E} = -\sum_i \frac{n_i}{n_e}\boldsymbol{V}_i \times \boldsymbol{B} + \frac{\boldsymbol{J} \times \boldsymbol{B}}{en_e} - \frac{1}{en_e}\nabla P_e + \eta(x)\boldsymbol{J} \tag{10}$$

[15] The first term in (10) is the ideal Ohm's law. The last term, $\eta(\boldsymbol{x})\,\boldsymbol{J}$, is added to allow for finite conductivity in the ionosphere only. Collisions beyond this region are assumed to be negligible. No anomalous resistivity is included in the code. The Hall and grad P terms in (10) are the same as in hybrid codes. Note that these latter corrections can drive electric fields in the plane of the ion velocity and therefore under the right circumstances can lead to the acceleration of the ions.

[16] In order to see how these effects are playing out in the plasma dynamics, consider the form of the individual

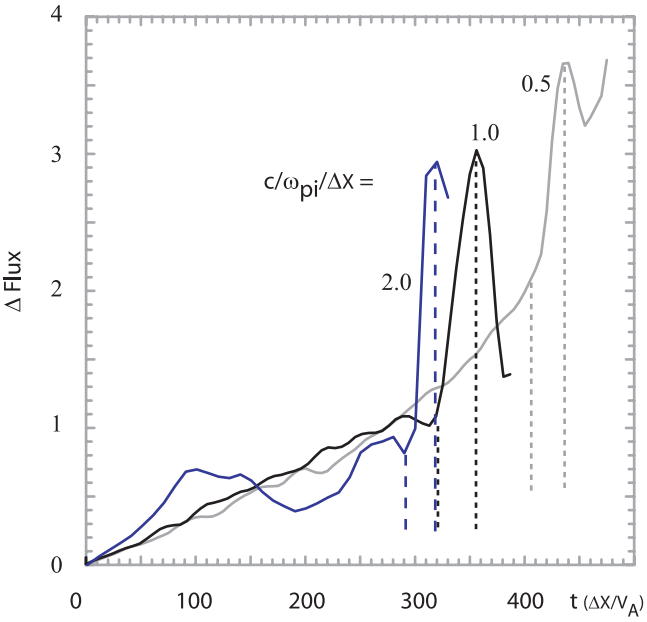

Figure 1. Reconnected flux for a one-dimensional (1-D) Harris current sheet as a function of time for a fixed width of 7.5 grids units. Each curve is for a different value of the ratio of ion skin depth to the grid spacing.

fluid momentum equations with (10) substituted in (2) yielding

$$\rho_\alpha \frac{d\boldsymbol{V}_\alpha}{dt} = q_\alpha n_\alpha \left(\boldsymbol{V}_\alpha \times \boldsymbol{B}(\boldsymbol{r}) - \sum_i \frac{n_i}{n_e} \boldsymbol{V}_i \times \boldsymbol{B} \right) + q_\alpha n_\alpha \left(\frac{\boldsymbol{J} \times \boldsymbol{B}}{e n_e} - \frac{1}{e n_e} \nabla P_e \right) - \nabla P_\alpha - \left(\frac{GM_E}{R^2} \right) \rho_\alpha \vec{\boldsymbol{r}} \tag{11}$$

The first term in (11) ($V_\alpha \times \boldsymbol{B} - \sum (n_i/n_e)\ V_i \times \boldsymbol{B}$) is dropped in MHD. If this is done a single species is assumed (11) reduces to the ideal MHD momentum equation. In reality the presence of different ion species or energy populations means that ($V_\alpha \times \boldsymbol{B} - \sum (n_i/n_e)\ V_i \times \boldsymbol{B}$) is invariably nonzero and this drives ion cyclotron effects, particularly at boundary layers and/or thin current sheets. The same difference occurs in hybrid codes where one has a difference in velocity of the individual ions relative to the bulk velocity generating a nonzero sum similar to the one in (11). This acceleration of ions can lead to conversion of magnetic field energy associated with a thin current sheet to particle kinetic energy.

[17] The dissipation for the reconnection described by the above equations has two contributions. The first is from the demagnetization of the ions, which can be accelerated by the electric field when their gyroradius is larger than the inherent scale size of the current sheet. With the resolution of the global code the electrons remain magnetized. In the idealized local geometry in section 2, magnetization of electrons can eventually lead to the suppression of reconnection. However, the second factor that contributes to the dissipation is that in the global model the field lines are tied to a resistive ionosphere. Magnetization of electrons is overcome by their transport along the magnetopause, into the cusp and eventual coupling to the ionosphere.

[18] For a tail current sheet with a density between 0.1 and 1 cm^{-3}, the ion skin depth ranges from 600 km to 200 km. The oxygen skin depth can be potentially 10 times larger. Similarly, the gyroradius of a 1-keV proton in the center of the current sheet where the magnetic field is of the order of 5 nT is about 600 km and that of O^+ at the same energy is 2400 km. Smaller scale lengths are relevant to the magnetopause where the densities are higher and the energies in general are lower. In the original multifluid simulations [*Winglee et al.*, 1998, 2005] the grid resolution was 0.25 R_E, which begins to capture the separation of the O^+ dynamics from the H^+ dynamics but the resolution is insufficient to resolve the demagnetization of the H^+ ions.

[19] In this paper refinement gridding is utilized to yield local grid resolutions of 200 km at the magnetopause. This is accomplished by first establishing a global equilibrium at coarse (1/4 R_E) resolution for nonsubstorm/nonstorm conditions. The refinement gridding system is then initiated around the region of interest to desired resolution and the system is then driven by the desired solar wind conditions. Plasma and field quantities are passed between grid systems at each time step ensuring full coupling between the grid systems. This makes the code not only multifluid but also multiscale and allows us to investigate for the first time the roles of different plasma components and external forcing on the reconnection within thin current sheet embedded in a global magnetosphere. It enables the tracking of the evolution starting from the turning of the IMF to tens of minutes or hours real-time. This timescale is to be compared with hybrid/kinetic local simulations that span at most a few tens of seconds for idealized geometries. *Harnett and Winglee* [2005] have demonstrated the importance of this technique for examining the thinning of the tail current sheet down to a thickness of 400 km with refinement gridding utilized 100 km grid resolution. Here we demonstrated thin current sheets at the magnetopause and the generation of flux ropes that are related to flux transfer events using grid resolution of 200 km at ±2 R_E around the subsolar magnetopause.

3. Model Predictions for a Harris Current Sheet

[20] Before discussing the results for the terrestrial magnetosphere, we first demonstrate that the code incorporates key characteristics of reconnection seen in idealized 2-D hybrid simulations of reconnection in a Harris current sheet. Two critical features of reconnection that have been firmly established in the literature are (1) that the reconnection in collisionless current sheets is associated with the development of an in-plane magnetic field that has a quadrupole distribution and (2) that the reconnection rate is rapid (of the order of 0.15 $V_A B_0$) [*Shay et al.*, 1999, 2001; *Karimabadi et al.*, 2004]. Here we demonstrate that this physics is incorporated in the multifluid code. A 1-D Harris current sheet is initialized with a half thickness $L = 7.5$ on a 2-D grid of 180 × 100. Our multifluid treatment shows this configuration is stable to reconnection, similar to the results of *Karimabadi et al.* [2004], and a small perturbation must be included to initiate reconnection. This perturbation is provided by a local region of resistivity with a Gaussian profile 100 × 50 with a peak Reynolds number of 20.

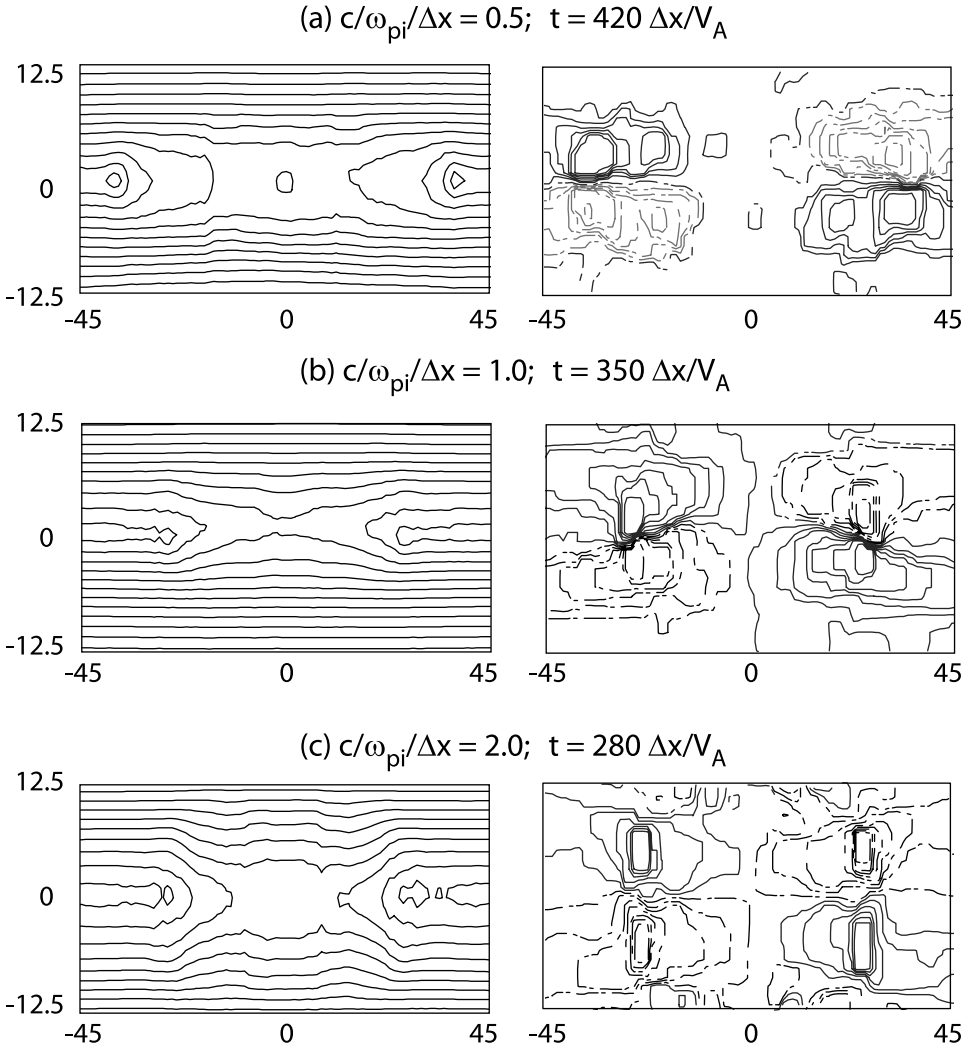

Figure 2. Magnetic field structure during the bursty reconnection events of Figure 1, with the field lines in the x-z plane shown on the left-hand side and the in-plane (B_y) field shown on the right-hand side.

[21] Figure 1 shows the reconnected flux for three different values of the ion skin depth, relative to the grid spacing. There is a slow increase in the reconnected flux due to the imposed resistivity. For the case where the ion skin depth is under resolved at half the grid spacing, a burst of reconnection occurs at t $\sim$ 400 $\Delta X/V_A$. As the ion skin depth is better resolved, one sees that the bursty reconnection appears earlier (i.e., the reconnection is controlled by a physical process) and that the characteristics of the reconnection for $(c/\omega_{pi})/\Delta X$ = 1.0 and 2.0 are fairly close together, that is, once the ion skin depth is resolved there is not a significant change in the dynamics.

[22] The reconnection growth rate can be estimated from the rise time of the fast reconnection. The dashed lines in Figure 1 show the estimated period where fast reconnection is occurring. There is some ambiguity in choosing the initial start of the fast rise, due to the slow rise from the underlying resistive process. This is particularly true for the case of $(c/\omega_{pi})/\Delta X$ = 0.5 and the dashed lines are at best a rough estimate, with the growth rate being about 45 ± 10 $\Delta X/V_A$. For $(c/\omega_{pi})/\Delta X$ = 1.0 and 2.0, the situation is less ambiguous with growth rates of 30–35 and 30–35 $\Delta X/V_A$, respectively. Noting that $(c/V_A) = \omega_{pi}/\Omega_i$, these periods correspond to 70–90/Ω_i, 30–35/Ω_i, and 15–20/Ω_i, respectively. This period is comparable to that derived by *Shay et al.* [2001], which has a rise time of about 40/Ω_i.

[23] There are two factors that contribute to the change in the growth rate between the cases. The first is that L is fixed in the above so that as $(c/\omega_{pi})/\Delta X$ increases, $(c/\omega_{pi})/L$ is increasing, that is, relative to an ion skin depth the current sheet in thinner, and the growth rate for increasingly thinner current sheets increases. The second factor is that the system size is effectively larger relative to the current sheet thickness and length as $(c/\omega_{pi})/\Delta X$ increases so that inhibition of reconnection from boundary conditions is also mitigated.

[24] The structure of the magnetic field during the bursty reconnection periods is shown in Figure 2. In all three cases, a quadrupole pattern can be seen in the in-plane (B_y) field. For the under resolved case of $(c/\omega_{pi})/\Delta X$ = 0.5, the B_y field antisymmetry line lies essentially along the current sheet, which is inconsistent with hybrid simulations. However, for the resolved cases of $(c/\omega_{pi})/\Delta X$ = 1.0 and 2.0, $|B_y|$ is maximized along the edges of the current sheet, and this is consistent with hybrid simulation results [*Shay et al.*, 2001].

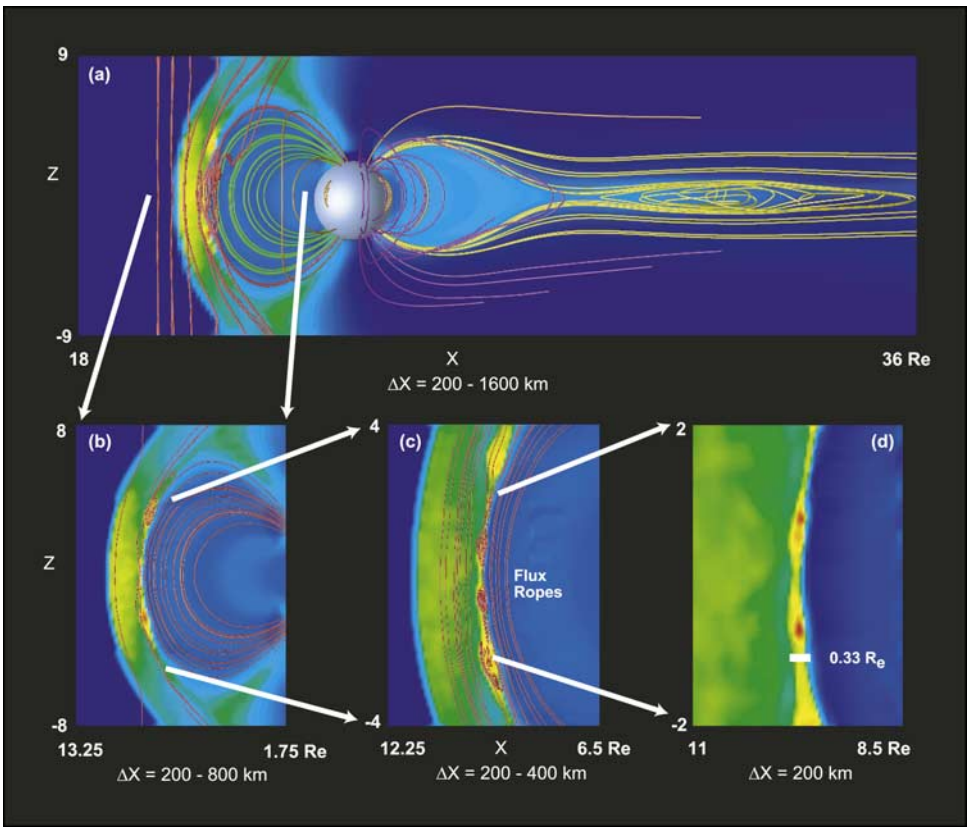

Figure 3. Structures along the magnetopause for southward IMF at high resolution. Contours show total electron plasma pressure along the noon meridian and the lines show mapping of magnetic field. Shown are (a) a global view of the magnetosphere and (b–d) just the dayside magnetopause at increasing resolution. A floating scale is used to highlight the features with the maximum pressure being seen at the smallest scale (Figure 3d) and is about 2 nPa.

The results for $(c/\omega_{pi})/\Delta X = 2.0$, appear better resolved but if one were to scale the images in terms of (c/ω_{pi}) instead of ΔX, the same overall geometry would be the same. In other words, while there may be some loss of resolution in the $(c/\omega_{pi})/\Delta X = 1.0$ case relative to the $(c/\omega_{pi})/\Delta X = 2.0$ case, the overall structure and reconnection rate are retained.

4. Magnetopause Flux Rope Global Features

[25] The localized treatments have limited application to the real magnetopause because they cannot determine the actual thickness that the current sheet would obtain before under going reconnection; the current sheet thickness is an input parameter A related problem is that there is no indication of whether the reconnection occurs through a single X-line or through multiple X-lines since this is also determined by the assumed initial geometry and the perturbation used to drive the initial reconnection. By using the multifluid/multiscale simulation, we can address these questions under realistic (as opposed to idealized) conditions. The global model was for run 2 h real time with regular resolution of 0.25 R_E and zero IMF (with solar wind density of 6 cm^{-3} and speed of 450 km) to establish an overall equilibrium for the magnetosphere. Refinement gridding was then imposed and the code continue to run for another 10 min to ensure the results were not affected by the refinement gridding. The finest gridding near the subsolar point was 200 km at $z = \pm 2$ R_E, and increasing to 400 km at ± 4 R_E and 800 km at ± 8 R_E. Southward IMF of -5 nT is introduced at the solar wind boundary at 0200 UT and reaches the magnetopause at about 0210 UT. The IMF and solar wind conditions are kept at these values from 0200 to 0245 UT.

[26] Figure 3a shows a global view of the magnetopause with close-up views of the subsolar magnetopause at ever-increasing resolution (Figures 3b–3d). The global magnetosphere closely resembles previous global model results with a well-defined magnetosheath, cusp, and magnetotail seen in the contours. There is a small reconnection region in the tail that arises from the fact that the IMF is zero up to this time. Tail reconnection will be the subject of another paper. The time shown in Figure 3 corresponds the first time reconnection starts to appear at the subsolar magnetopause. At the magnetopause there is some suggestion of a twisting of the field lines, which becomes more evident as one moves to the higher-resolution images (Figures 3b–3d). The twisting of the field is associated with flux ropes (Figure 3c), where closely wound spirals are evident. In addition to the flux ropes that are initiated near the solar point there are two additional flux ropes that developed near $z = \pm 3$ R_e (Figure 3b). These higher-latitude flux ropes arise from the fact that the solar wind forces the IMF transition across the entire magnetopause, that is, reconnection is not

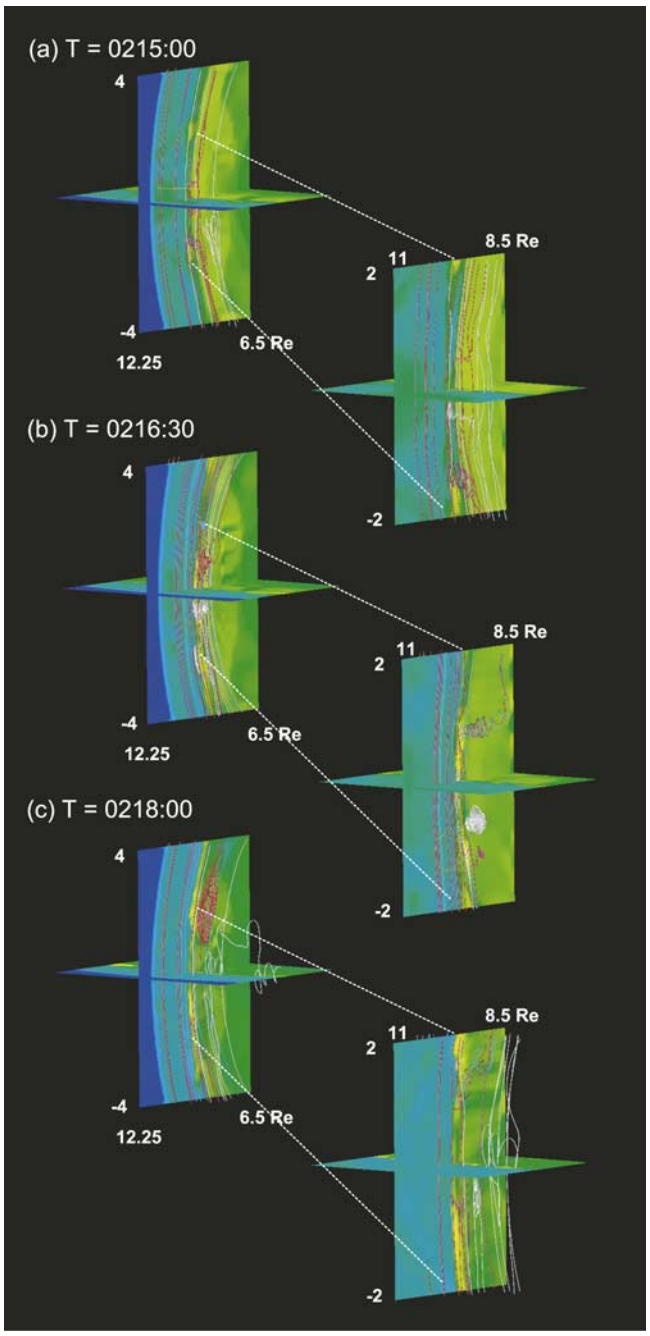

Figure 4. The left-hand side shows a 3-D perspective of the flux rope in Figure 3 at 400 km resolution. The right-hand side the flux ropes at 200 km resolution. The flux ropes are initiated near the subsolar region with relatively weak core magnetic field (T = 0215:00) and then intensify their core magnetic field (T = 0216:30) and then propagate to higher z so that it is not present in the high-resolution section at T = 0218:00 though is visible on the large view on the left-hand side.

restricted to the subsolar region but can occur several R_E off the equator, and there is multiple O-line reconnection occurring. The picture of the magnetopause is similar to *Dubinin et al.* [1977] where there is multimagnetic island formed along the magnetopause, and a single X-line typical of global MHD models is not seen. One difference is that there are only four islands formed and not the nearly 10 envisaged.

[27] Each of the flux ropes is associated with enhanced localized plasma transport in the north/south direction as seen by the two peaks in the plasma pressure (Figure 3d). These pressure enhancements are very small in scale size; at their widest they are about 0.33 R_E in width, and at their thinnest only about 600 km which is marginally resolved with grid resolution of 200 km in the region. It is important to note that these structures are smaller than typical grid resolutions of many present global simulations.

[28] Figure 4 shows the temporal and spatial evolution of the flux ropes. One difference with Figure 3 is that the pressure of the ionospheric protons is shown as opposed to the total pressure. This change in format shows that the magnetospheric side of the magnetopause is also involved in the formation of the flux rope (albeit at only <1% of the solar wind pressure at the magnetopause). At initiation (Figure 4a) the flux ropes have a longer extend in y (about 1 R_E) and the extent of the core magnetic field is only a small fraction of the structure. For example, the z-dimension of the flux ropes near the equator in Figure 4a is very much smaller than the more developed rope in at low z (about

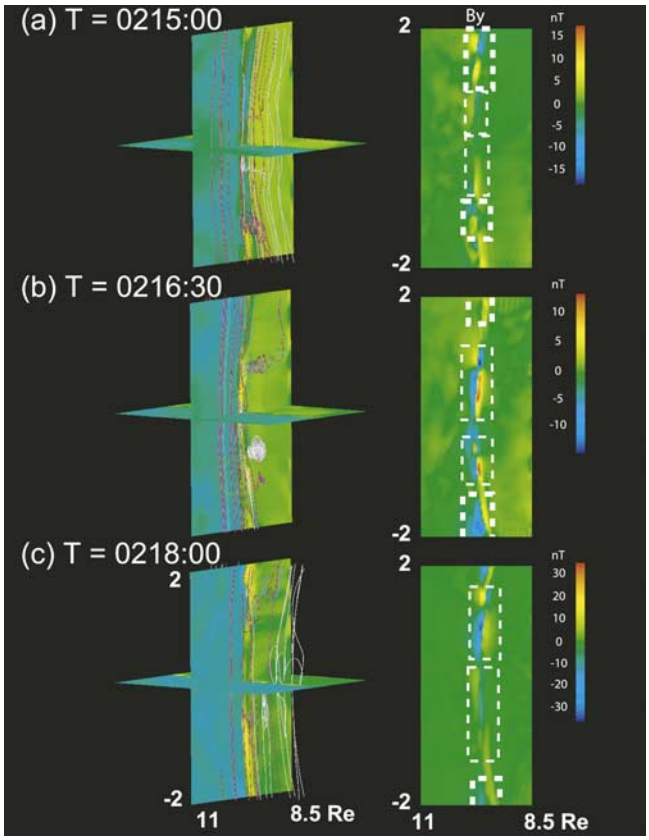

Figure 5. The left-hand side shows the 3-D representation of the flux ropes at the subsolar point within the highest grid resolution area, and the right-hand side shows contours of B_y along the noon-midnight meridian. The white boxes indicate sets of quadrupole associated with different flux ropes. The color bar on the right-hand side gives the values for B_y.

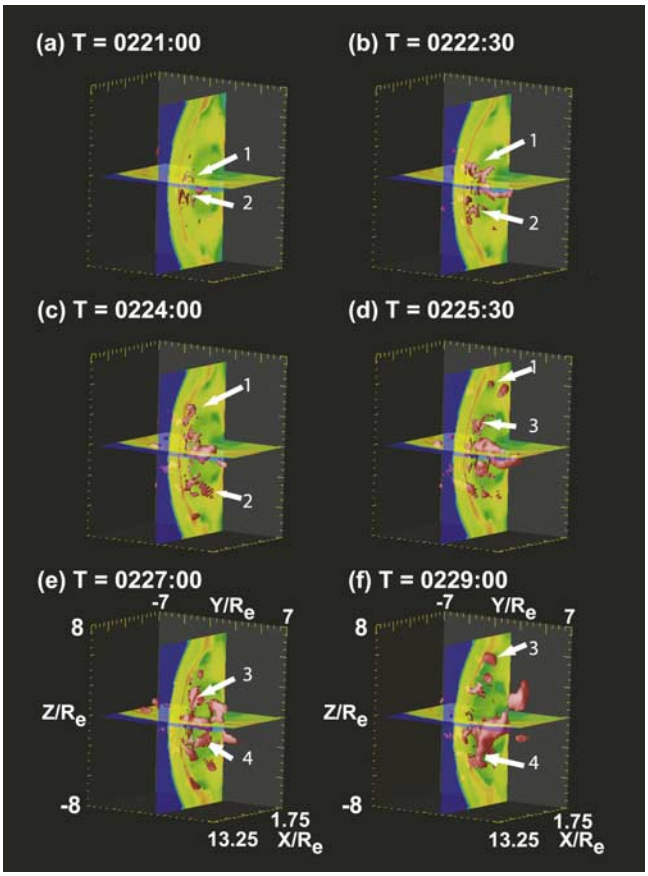

Figure 6. Three-dimensional development of the magnetic islands as seen through fixed isosurface of plasma pressure, with the contours in the noon-midnight and equatorial planes indicating the overall position of the magnetopause and bow shock. The numbers indicated the development of individual islands as they expand laterally and move to higher latitudes.

$\sim$0.33 R_E). As these flux ropes develop in size, the diameter and pitch of the flux ropes increases, indicating that both the strength and region over which a strong core field is present increases as the flux ropes develop and moves along the magnetopause. The large flux ropes of Figure 4b are seen to continue to grow in size, particularly the one in the northern hemisphere (Figure 4c) as it moves along the magnetopause. At the later stages of development the z extent is comparable its y extent, and the flux rope itself changes from a U-shaped to a V-shaped configuration (e.g., Figures 4b and 4c, right) as the core magnetic field becomes relatively stronger.

[29] One of the important issues for reconnection is the problem of magnetization of the electrons. In the global model as seen in Figures 3–4, reconnection occurs in association primarily with ion acceleration, and the size of the flux rope does not grow indefinitely as seen in the global view of the magnetospheres. The electrons that are frozen to the field are transported out of the region with these flux ropes as seen by localized enhancements in their pressure. Once the flux rope propagates out of the region, reconnection again occurs with new flux ropes being generated and the process is repeated. The observable signature of this repetitive process is discussed in the next section.

[30] The flux ropes/magnetic islands of Figure 4 are associated with the quadrupole magnetic field as demonstrated in Figure 5. For reference the left-hand side shows the images of the flux ropes over the highest resolution area, while the right-hand side shows contours of B_y along the noon-midnight meridian. The white boxes indicated approximate regions corresponding to each quadruple set. Because of the finite extent of the quadrupole components there is some merging of these components with adjacent flux ropes, so that there are some ambiguities in identifying individual quadrupoles. Nevertheless, the overall structure within each box has the basic structure as the idealized case of Figure 2, showing that the code is indeed capturing key Hall effects in the magnetic field around the reconnection site, and the reconnection is driven by physical processes and not arbitrary magnetic resistivities. The B_y component is seen to intensify with the development of the flux rope as it moves away from the subsolar region. Note also that the field is non-negligible with field strengths of the order of 10–20 nT. Similar magnitude field strength in B_y are also seen off the noon-midnight meridian emphasizing that the 3-D nature of the problem cannot be neglected.

[31] This off-axis development is illustrated in Figure 6 which shows the spatial evolution of the pressure enhancements associated with the flux ropes. Contours are given in the noon/midnight meridian and in the equatorial plane, while the isosurface is a set at a fix value close to the maximum (ionospheric) pressure in the region. Successive enhancements are indicated by the arrows/numbers. In addition to moving in the north/south directions there is expansion of the system of flux ropes from the dawn direction to the dusk side. Figures 6a and 6b show such an expansion over a couple of R_E, where it collides with another group of flux ropes, resulting in a convoluted structure that extends over 4 R_E in y. However, the northerly extension of Enhancement 1 is seen to break away (Figure 6c) and enter the cusp (Figure 6d). Enhancement 2 does not become as well organized. Instead a large equatorial group is seen to expand around toward the duskside. This pattern of discrete islands being formed, some of which propagate into the cusp and some of which coalesce with expansion to the dusk side is seen to repeat as shown in Figures 6e and 6f, leading to a quasi-periodic creation and ejection of the flux ropes from the subsolar region. The expansion in the dusk direction is consistent with ion acceleration in the direction of the magnetopause current.

[32] Another important feature of the flux ropes of Figure 4 is that they tend to extend from near the noon-midnight meridian toward the duskside and not the dawnside. As a result, a strong dawn/dusk asymmetry develops with the largest flux ropes expected to be observed preferentially on duskside. This asymmetry is also seen in Figure 6 where the pressure enhancements primarily lie on the duskside, and only a few small developing flux ropes appear on the dawnside.

[33] This dawn/dusk asymmetry is due to ion cyclotron effects. As noted in the discussion of the model equations, the electric field includes Hall and grad P terms. These corrections become important for thin current sheets and are

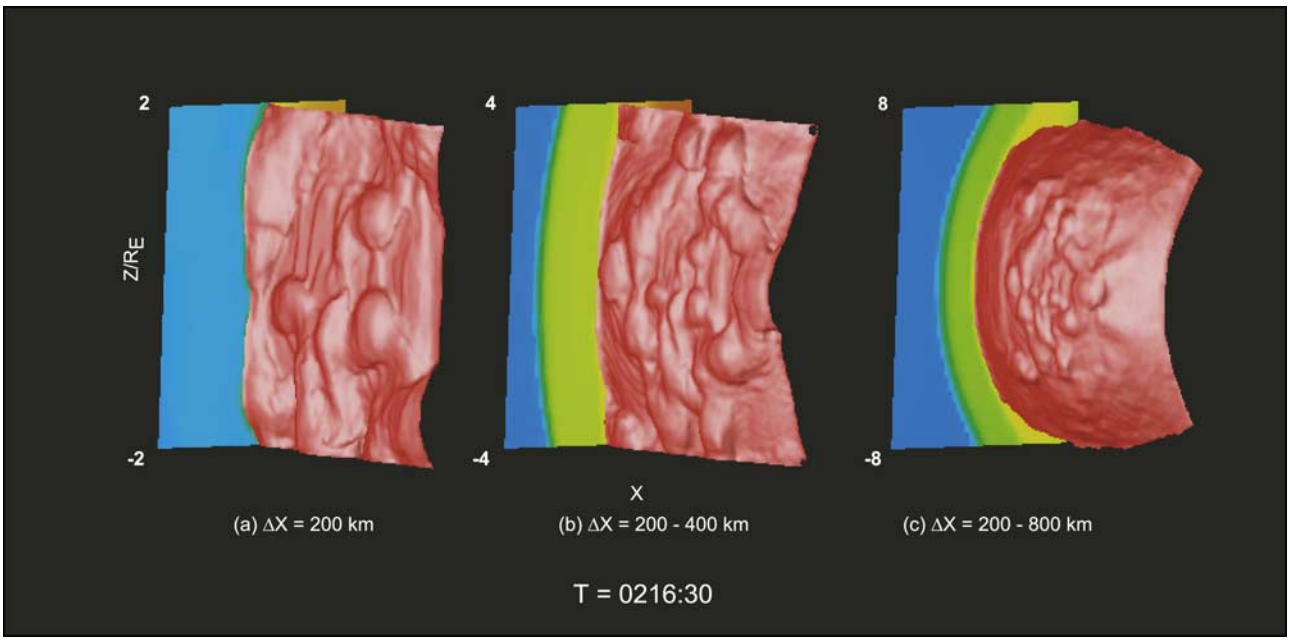

Figure 7. Rippling of the dayside magnetopause as seen at increasing larger perspectives from z = (a) ±2 R_E, (b) ±4 R_E, and (c) ±8 R_E for a fixed time of t = 0216:30. Contours of ionospheric plasma density are shown, and the isosurface intensity is reduced from that in Figure 6 so that the full magnetopause surface is captured.

responsible for the generation of the core magnetic field associated of the flux ropes as demonstrated in Figure 5. In addition, the $\boldsymbol{V} \times \boldsymbol{B}$ component of the electric field produces a component in the dawn/dusk direction so that $\boldsymbol{E} \cdot \boldsymbol{B}$ is nonzero. These magnetic and electric field components in the presence of ions that have a gyroradius comparable to the current sheet thickness leads to the acceleration of the plasma from the dawnside to the duskside.

[34] The presence of multiple flux ropes at any one time causes the surface of the magnetopause to be highly rippled or bubble as illustrated in Figure 7. This figure shows an isosurface of the ionospheric proton pressure, which gives an indication of the location of the magnetopause surface at least as determined from the presence of magnetospheric plasma. As in Figure 3 a single snapshot is shown at three different scales sizes. At the highest resolution the magnetopause as identified in this manner has variances possibly extending out as much as 1000–2000 km from nominal flat surface. This rippling is concentrate to several R_E around the subsolar point (Figures 7a and 7b). Beyond this region (Figure 7c) the rippling is less strong. There are two potential reasons for this reduction in strength. First, there is limited grid resolution at large distances (going from 200 km at the subsolar region to 800 km near the terminator). A full coverage of the entire magnetopause at high resolution is beyond our capabilities at this time. The second reason is that the boundary layer is also thicker at large distances, and as such the flux ropes would not appear as a large perturbation as the cusp in approached. The important point is that regardless of the high latitude dynamics, the magnetopause near the subsolar region is not the smooth magnetopause of the *Dungey* [1963] or global MHD, but instead it is the rippled surface suggested by the multi-X line models, and this rippling has implications for spacecraft observations as described in section 5.

5. Flux Rope Signatures

[35] The fact that the model indicates the presence of multiple flux ropes and the rippling of the magnetopause at scale sizes of 400–1600 km has important consequences for the understanding spacecraft observations of the magnetopause. In this section we show potential signatures that would be observed during an idealized magnetopause encounter. Observed features of flux transfer events and magnetopause crossing are reviewed by *Russell* [1989] and *Elphic* [1989]. These signatures include multiple crossing of the magnetopause during a typical spacecraft encounter with the magnetopause, with associated changes in magnetic field and plasma density and speed. As discussed below, even for the idealized IMF conditions considered here, the multifluid/multiscale model is able to capture many features identified in the above reviews.

[36] For simplicity we consider two spacecraft: (1) spacecraft 1 at $\boldsymbol{r_1}$ = (9.25, 0., 0.) R_E near the subsolar point and (2) spacecraft 2 at $\boldsymbol{r_2}$ = (9.75, 0.5, 0.) R_E at slightly larger radial distance and displaced by 0.5 R_E in the dusk direction. The magnetic field and plasma properties are sampled continuously during the simulation. The displacement in the dusk direction was included to capture effects associated with the duskward expansion of the flux ropes. Without refinement gridding these spacecraft would be separated by a couple of grid points and variations in macroscopic quantities would be closely correlated. With the refinement gridding as demonstrated in the following, the spacecraft can encounter very different physical conditions.

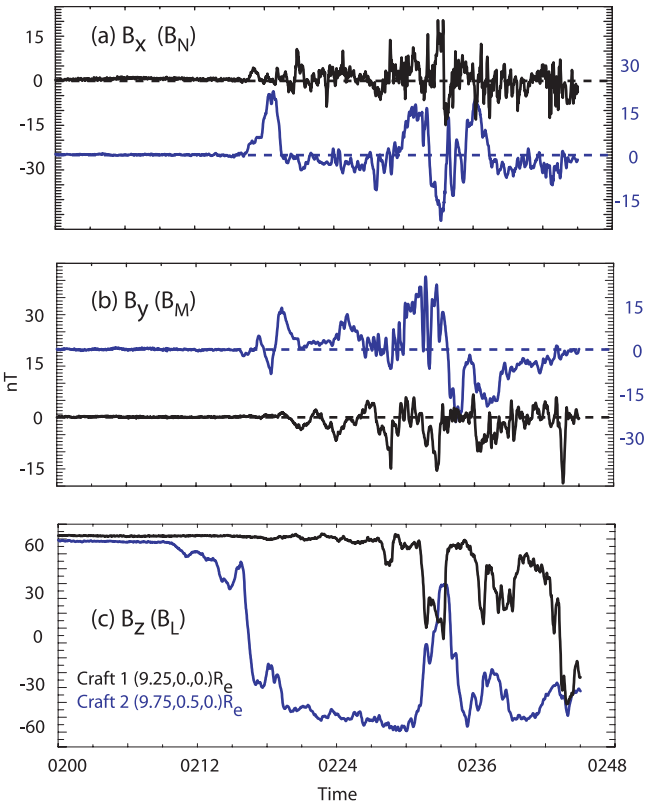

Figure 8. Time evolution of the magnetic field components at two fixed points: (9.25, 0., 0.) R_E (black line) and (9.75, 0.5, 0.) R_E (blue line). These time histories represent pseudo-spacecraft that are displaced by 0.5 R_E in x and y. Despite the relatively small displacement (at least by global simulation standards), they see markedly different signatures depending but occasionally sample the different sides of a single FTE feature.

[37] Figure 8 shows the magnetic field signatures for the two spacecraft. The quantities are left in Cartesian coordinates. Because of the position of the spacecraft are very close to the subsolar point, in a boundary normal coordinate system (*LMN*), L is essentially along the z axis, M along the y axis and N along the x axis. The B_z signature (Figure 8c) for the two spacecraft is simplest to interpret. Initially, both spacecraft are inside the magnetopause (strong positive B_z), which is beyond 9.75 R_E for zero IMF. As the IMF becomes southward the magnetopause moves inward, with spacecraft 2 moving from the magnetosphere into the magnetosheath. The crossing starts at about 0210 and spacecraft 2 is not fully though the magnetosheath until 0218. However, spacecraft 2 reencounters the magnetosphere at 0233 and to a lesser extent at 0238.

[38] In contrast, spacecraft 1 does not fully enter the magnetosheath until 0243 and it does so within a minute. Prior to this magnetopause crossing, spacecraft 1 has encounters with the magnetopause boundary layer at 0228, 0232–0234, 0236–0239, and 0243–0245. In other words, despite the fact that the solar wind, IMF, and spacecraft positions are constant both spacecraft have multiple encounters with the magnetopause boundary layer. Such multiple crossing are often observed during spacecraft encounter of the magnetopause [*Russell*, 1989; *Elphic*, 1989].

[39] These boundary layer encounters are associated with flux rope structures as seen by the spikes in B_y in Figure 6b. Spacecraft 1 (which is primarily on the magnetospheric side of the magnetopause) primary sees bipolar swings in B_y though the negative component is larger. This B_y originates from the Hall term in the generalized Ohm's law. In the shallower magnetopause encounters by spacecraft 1, the B_y is only a small fraction of the magnetic field, while during the deeper encounters at 0233 and 0244 the B_y component is comparable in magnitude to the B_z component. There is very little curvature in the normal direction on the magnetospheric side at spacecraft 1 as evidence by the only small (<5 nT) perturbations in B_x signature. There is, however, a well-defined bipolar swing at 0233 and a weaker one at 0227.

[40] For comparison, spacecraft 2, being on the magnetosheath side of the structures, sees both unipolar and bipolar swings in B_x and B_y. The swings can be either opposite to that seen by spacecraft 1 (e.g., prior to 0233) or can have the same sign and shape as spacecraft 1 (e.g., after to 0234). In addition, spacecraft 2 sees a lumpy magnetopause with several large swings in B_x. In other words, there is much stronger curvature to the flux ropes on the magnetosheath side than on the magnetospheric side. This difference is curvature is consistent with the pressure contours of Figure 3a and yields a configuration similar to the schematic of an FTE developed by *Elphic* [1989, Figure 6].

[41] The corresponding bulk velocity of the plasma is shown in Figure 9. When both spacecraft are inside the magnetosphere they measure small sunward convection with V_x < 10 km/s. When spacecraft 2 crosses into the magnetosheath proper sees an earthward flow of 30–40 km/s, while at the same time spacecraft 1 sees enhanced sunward speeds up to about 20 km/s. During transient encounters with the magnetopause boundary layer speeds up to ±80 km/s can be seen in association with the rippling of the magnetopause as discussed in the previous section, and their timing flux rope signatures in the magnetic field data of Figure 8.

[42] In contrast, much higher speed flows are present in the north/south direction (Figure 9c) associated with acceleration out of the reconnection region. The highest speed flows are seen by spacecraft 1 on the magnetospheric side of the boundary layer. This asymmetry is present because of the small mass density present on the magnetospheric side. These flows can reach speeds comparable to the solar wind speed of about 450 km/s (Figure 9c). These flows also have a significant dusk component (Figure 9b) even though the spacecraft is at the subsolar point. In ideal MHD these flows would have to be in the north/south direction only. The magnitude of these bursts of enhanced speed and the fact that they occur in all three velocity components and the duration over which they occur is very similar to the observations reported by *Elphic* [1989, Figure 8].

[43] Both spacecraft see predominantly positive V_y, consistent with expectations from current sheet acceleration. Spacecraft 1 occasionally see very strong positive enhancements in V_y associated with FTE encounters. Spacecraft 2 on the magnetosheath side sees opposite signed enhancements in V_y associated with some but not all its FTE encounters.

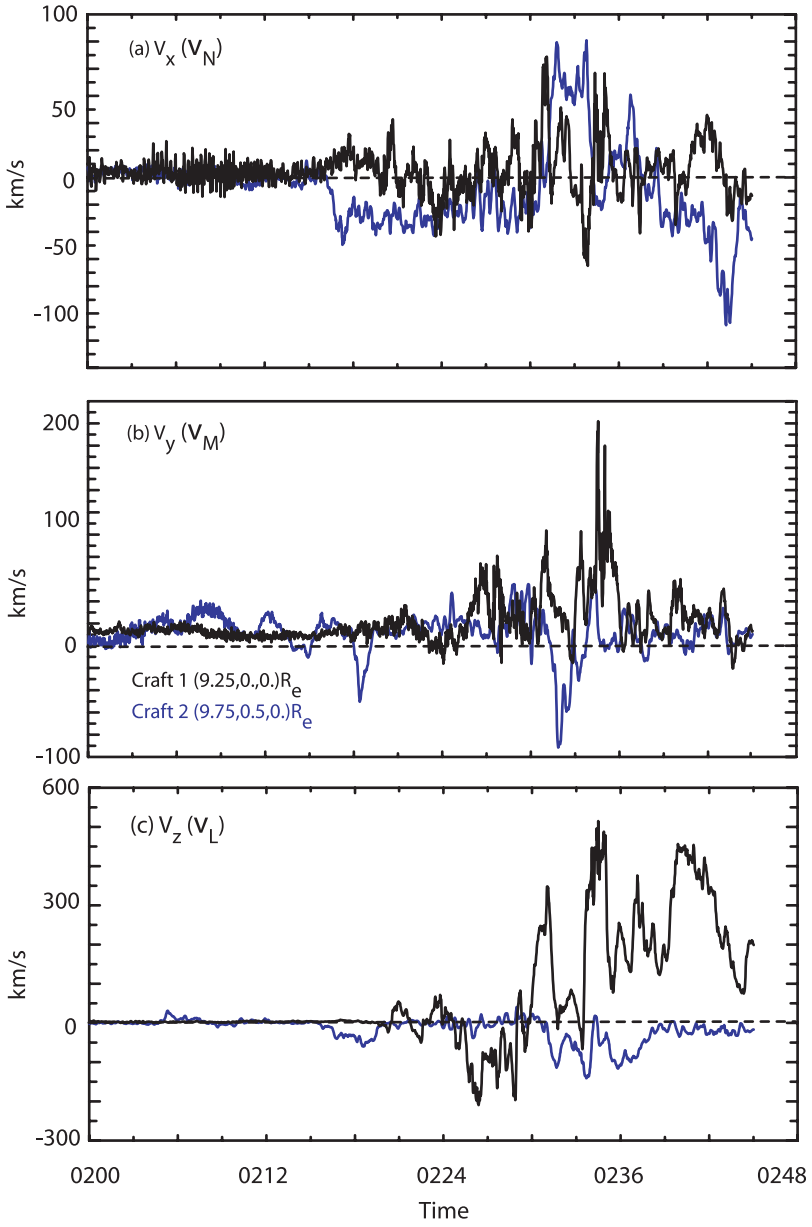

Figure 9. Same time evolution as in Figure 8, except the plasma velocity components are shown. Enhanced speeds in all three components are seen in association with FTE encounters.

The negative enhancements result from some of the accelerated plasma gyrating out of the current sheet. Consequently, the structure of the FTEs is very much more complicated in 3-D than the simple idealized simulations of section 2 would suggest, but this structure provides observable signatures for quantify reconnection at the magnetopause.

[44] The contributions to the density observed by the two spacecraft are shown in Figure 10. Only the proton contributions to the density are shown because the O^+ density for the parameters considered here is not significant at 0.25% relative density and its time profile is very similar to the ionospheric H^+ density. Since spacecraft 2 enters the magnetosheath first this entry is accompanied by enhanced density of solar wind plasma (Figure 10a). Note though that the solar density fluctuations encountered by the spacecraft after its magnetopause crossing at 0218 are relatively at less than a factor of 2 (Figure 8a). On the other hand, spacecraft 1 sees much large fluctuations which start before its full entry into the magnetosheath (at least as determined by the magnetic field signatures in Figure 8). For example at 0233 it sees densities similar to spacecraft 2, even though B_z at this time is almost zero; that is, the spacecraft is not completely into the magnetosheath. Enhanced magnetosheath density while not fully across the magnetopause is consistent with the AMPTE results of *Elphic* [1989].

[45] The converse is true of the plasma of ionospheric origin (Figure 10b). Spacecraft 1 sees strong fluctuations in this density component even though, as noted above, it is primarily in the magnetosheath. These fluctuations are therefore signatures of leakage of magnetospheric plasma into the magnetosheath. This result is consistent with the schematic developed by *Gosling et al.* [1990] showing entry

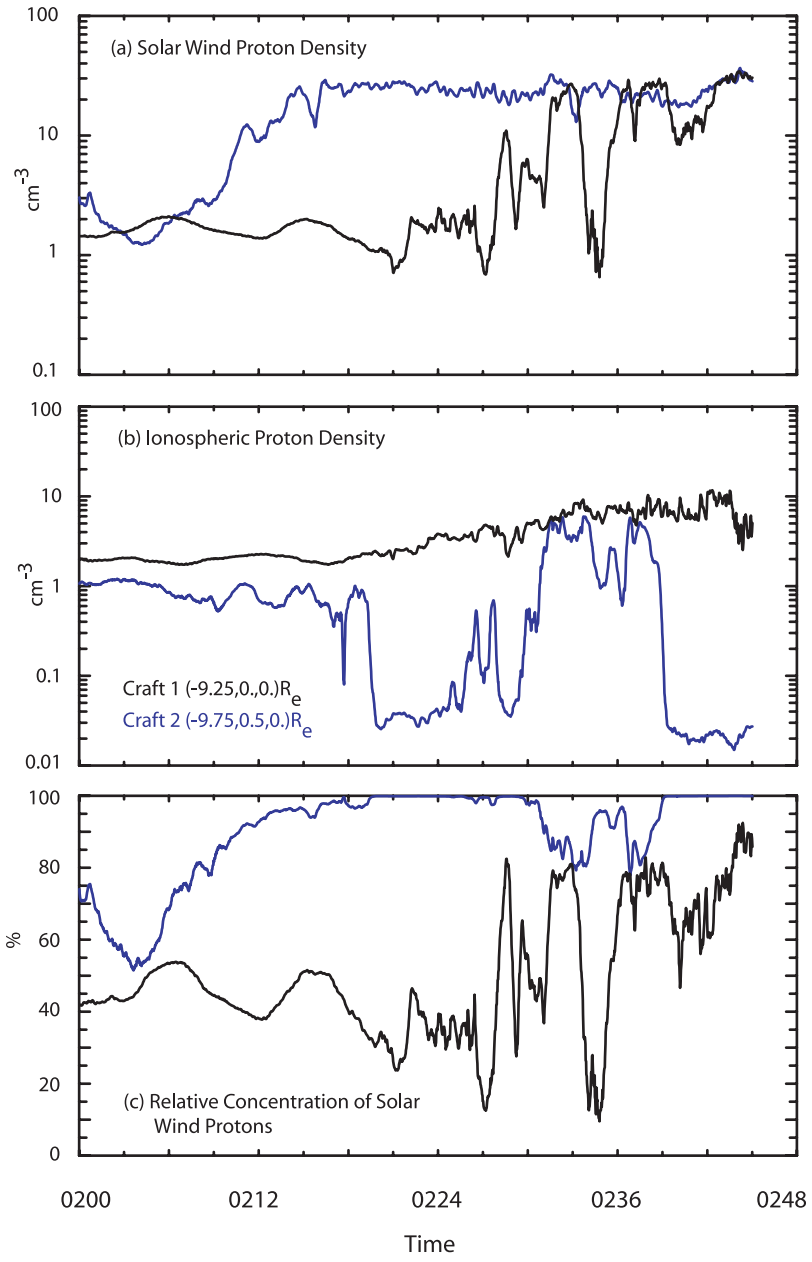

Figure 10. Evolution of the density of (a) solar wind origin, (b) ionospheric origin, and (c) the relative density of solar wind plasma at the two space positions. The FTE events are seen to correspond with large swings in the solar wind density if the spacecraft is on the magnetospheric side of the feature, and in the ionospheric density if the spacecraft is on the magnetosheath side of the FTE.

of magnetosheath particles into the magnetosphere and leakage of magnetospheric particles into the magnetosheath. The modeling presented here shows that the development of the FTE leads to enhancement magnetospheric leakage and enhanced solar wind entry. Thus if one looks at the relatively density profile (Figure 10c), spacecraft 2 on the magnetosheath side sees large swings in plasma of ionospheric origin but little magnetosheath variations, while spacecraft 1 on the magnetospheric side sees the exact opposite with little variations in the magnetospheric plasma but large swings in the plasma of solar wind origin.

[46] Another feature seen in Figure 10b is that spacecraft 1 sees an increasing amount of ionospheric plasma before it crosses the magnetopause. This increase is due to enhanced sunward convection on the dayside magnetosphere under southward IMF, which drives an increase in the cross-polar cap potential. This enhanced density changes nearly a factor of 5 over a period of about 50 min of southward IMF. This enhanced density is important because it means that the properties of the FTEs at the start of the southward turning will be different from those during sustained southward IMF, at least it terms of composition.

[47] Resolving the dynamics at the magnetopause is important as it determines the characteristics of the mass and momentum from the solar wind that is coupled to the terrestrial magnetosphere. Development of accurate models

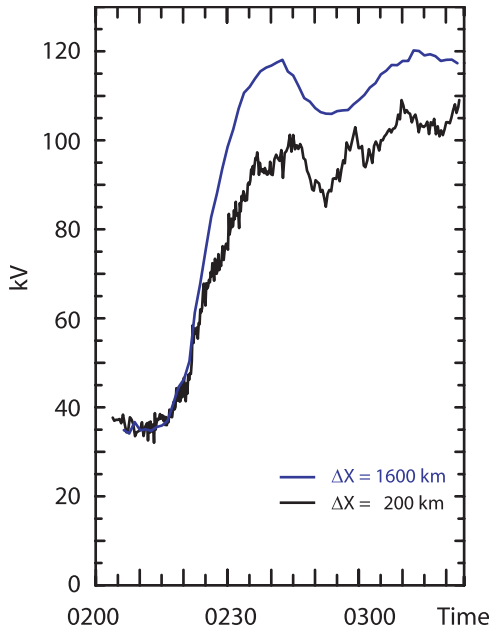

Figure 11. Cross-polar cap potential as derived for the simulations without refinement gridding (blue line) and with refinement gridding (black line). Resolution of the dynamics at the magnetopause leads to a 20% reduction in the cross-polar cap potential.

for magnetospheric activity such as substorms and storms will remain difficult until this dynamics is fully resolved. One area where a major difference in results is seen in the cross-polar cap potential, as shown in Figure 11. Simulations with 1600 km resolution and no refinement gridding and run under exact the same solar wind and IMF conditions yield a cross-polar cap potential of 120 kV. With refinement gridding, the cross-polar cap potential is seen to drop by nearly 20%. Since the main contribution to the cross-polar cap potential is from the convective term of the electric field, this means that on average the speeds at which plasma is moving within the magnetosphere is reduced by 20%. As a result, trying to predict the timing of important magnetospheric features like substorm onset could be off by amount of 20%. Additional effects may be found when the dynamics of the tail is resolved at similar spatial scales as the work described here.

6. Summary and Conclusions

[48] An important factor in collisionless reconnection is the ratio of the ion skin depth to the thickness of the current sheet. When this ratio is near one, the Hall term in the generalized Ohm's law becomes important which leads to fast reconnection and the development of a quadrupole or core magnetic field in the plane of the current. These effects are demonstrated to be present in the multifluid/multiscale method as illustrated by the 2-D simulations of the Harris current where these effects have been previously well documented. In these idealized geometries, a perturbation either from localized anomalous resistivity or some perturbation to the convective electric field is required produce the initial reconnection.

[49] The multifluid/multiscale simulations are able to move beyond the above idealized local case studies to a full treatment of the global magnetopause with high resolution around the magnetopause. This treatment is important as it allows a self-consistent treatment of the coupling of global processes associated with convection in a 3-D magnetosphere to the small-scale (ion cyclotron and ion skin depth) processes without the need for assuming any artificial anomalous resistivity. Inhomogeneities along the magnetopause are a natural consequence of a round magnetosphere interacting with a planar disturbance in the IMF-transit time effects ensure that there are always some regions that experience the IMF changes more strongly or at different times to other regions. This difference in forcing automatically sets up inhomogeneities in the magnetosphere.

[50] The inhomogeneities in the magnetopause current sheet allows for the formation of multiple magnetic islands. For the assumed solar wind conditions, four such islands develop initially. These magnetic islands, like the idealize simulations of the Harris current, have the quadrupole in-plane magnetic field stemming from the Hall effect, yielding a flux rope structure in 3-D that are initially only a fraction of an R_E in width. The 3-D simulations go further than the idealized 2-D simulations by showing that these flux rope structures will expand laterally (dawn/dusk) to a few R_E as they move poleward, with magnetic islands forming over a few R_E region in the north/south direction. Some of the magnetic islands are seen to coalesce, with the thickness of the magnetopause varying from a few hundred km to a few thousand kilometers, and the thickness of the full region being associated with the largest magnetic islands.

[51] The presence of these fluxes ropes leads to the rippling of the magnetopause, as opposed to the smooth magnetopause surface that is typical of global MHD models. This rippling means that a slow moving spacecraft will have multiple magnetopause crossing even under steady solar wind conditions, with the depth of penetration dependent on the size of the flux rope and its displacement relative to the spacecraft.

[52] An important feature of the model is that it is able to reproduce the quadrupole in-plane magnetic field component seen in local particle simulations. An individual spacecraft or closely spacecraft will typically only cross one side of the quadrupole and therefore see a bipolar signature if it crosses perpendicular to the current sheet and unipolar signature for diagonal encounters. While efforts to reconstruct the flux rope structure from spacecraft observations [e.g., *Sonnerup et al.*, 2004] have been successful in reproducing the bipolar signature, the magnetic topology assumed in such modeling efforts does not take into account the quadrupole nature of the induced magnetic field. One difference that does arises is that in the strict dipole geometry of *Sonnerup et al.* [2004] the center of the flux rope has a local maximum in field intensity and a local minimum in plasma pressure. In the presence of the quadrupole field configuration in the modeling presented here the opposite is true; the flux ropes are associated with a peak in the plasma pressure and a local minimum in field strength.

[53] The characteristics of the magnetopause and the flux ropes within it as derived by the model have several features

consistent with observed properties including (1) the size of the flux ropes at few hundred to a thousand km, (2) the curvature of flux ropes which is more highly curved on the magnetosheath side than on the magnetospheric side, (3) core B_y magnetic fields that are comparable to the B_z component, (4) high-speed flows in the z direction, along with moderate speed flows in the x and y directions, (5) interaction times of less than about a minute with a quasi-periodic recurrence rate of several minutes, and (6) the density on the magnetosheath side of the flux rope shows strong variations in the density of ionospheric/magnetospheric plasma, and on the magnetospheric side, there are strong variations in the density of plasma of solar wind origin. These density variations also demonstrate the entry of solar wind plasma into the magnetosphere and the leakage of magnetospheric plasma into the magnetosheath, which is also a key feature of FTEs. It is only through the coupling of small-scale processes within a global code developed here that convergence between observations and modeling can start to be obtained.

[54] The influence of these small scale processes does have an effect on the global magnetosphere. Besides determining the entry of solar wind and magnetosheath plasma, it is shown that the cross-polar cap potential drops by about 20% when high resolution at the magnetopause is included. One might consider it good news that the effect is only 20% but in a substorm with a growth period of 45–60 min, this difference means that there is a 20% error in the bulk flow of plasma in the magnetosphere that could lead to timing errors as large as 10 min, making detailed model/observational studies problematic at best.

[55] The presence of a strong core magnetic field has important consequences that need to be further studied beyond the results presented here. In particular, the issue of whether anti-parallel or component reconnection occurs for a nonzero B_y in the IMF is presently being debated. This debate has the implicit assumption that the magnetopause is smooth so that one can separate out the magnetosheath field from the magnetospheric fields. For a magnetopause that is rippled by FTEs this question may not be the right question. In particular, as we have seen when the reconnection region is resolved so that Hall effects become important, a quadrupole core magnetic field component develops that extends well beyond the reconnection region. As a result, even though the IMF may have an unaligned magnetic component with a smooth magnetopause, the Hall reconnection fields have the potential to produce a local canceling of the unaligned component and enabling anti-parallel reconnection to occur in a region that nominally would not be able to support anti-parallel reconnection. Such effects will be addressed in future work.

[56] As a final note, this paper has concentrated on interactions during for the first 45 min of the magnetopause dynamics after the arrival of southward IMF. We have also investigated the interaction out to timescales twice as long, but the physical processes involved become much more complex. We do note that on longer timescales the cross-polar cap potential for the high-resolution run remains 20% on average below the low-resolution run. The reconnection rate though becomes complicated by magnetospheric/ionospheric coupling. This coupling includes an increase in the density of the cold ionospheric plasma being convected out from the plasmasphere and into the magnetopause. This increase in ionospheric density is seen in Figure 10 and can lead to suppression of reconnection, since the presence of cold plasma will tend to decrease both the average ion skin depth and ion gyroradius of the ions at the magnetopause. Substorm activity though can lead to the injection/transport of energetic ions as well as heavy ionospheric ions into the dayside and eventually to the magnetopause. This plasma would on average increase the average gyroradius and enhance reconnection. Which of the two effects actually dominates is highly dependent on the actual prevailing solar wind conditions. Because of this sensitivity we are unable to document these processes in this already long treatise, and a thorough investigation is still needed in the future.

[57] **Acknowledgments.** This work was support by NASA grant NNG05GM39G and NSF grant ATM 0617654 to the University of Washington.

[58] Amitava Bhattacharjee thanks Thomas Penz and another reviewer for their assistance in evaluating this paper.

References

André, M., A. A. Vaivads, S. C. Buchert, A. N. Fazakerley, and A. Lahiff (2004), Thin electron scale layers at the magnetopause, *Geophys. Res. Lett.*, *31*, L03803, doi:10.1029/2003GL018137.

Berchem, J., and C. T. Russell (1982), The thickness of the magnetopause current layer: ISEE-2 and -2 observations, *J. Geophys. Res.*, *87*, 2108.

Birn, J., et al. (2001), Geospace Environmental Modeling (GEM) magnetic reconnection challenge, *J. Geophys. Res.*, *106*, 3715.

Biskamp, D., E. Schwartz, and J. F. Drake (1995), Ion-controlled collisionless magnetic reconnection, *Phys Rev. Lett.*, *75*, 3850.

Drake, J. F., R. G. Kleva, and M. E. Mandt (1994), Structure of thin current layers: Implications for magnetic reconnection, *Phys Rev. Lett.*, *73*, 1251.

Dubinin, E. M., I. M. Podgorny, and Y. N. Potanin (1977), Experimental proof of the existence of open and closed models of the magnetosphere, *Kosmich. Issled.*, *15*, 866.

Dungey, J. W. (1963), The structure of the exosphere or adventures in velocity space, in *Geophysics of the Earth's Environment*, edited by C. De Witt et al., pp. 505–550, Gordon Breach, New York.

Elphic, R. C. (1989), Observations of flux transfer events: Are FTEs flux ropes, islands, or surface waves, in *Physics of Magnetic Flux Ropes*, *Geophys. Monogr. Ser.*, vol. 58, edited by C. T. Russell, E. R. Priest, and L. C. Lee, p. 455, AGU, Washington, D. C.

Fu, Z. F., and L. C. Lee (1986), Multiple X line reconnection. II. The dynamics, *J. Geophys. Res.*, *91*, 13,373.

Gosling, J. T., M. F. Thomsen, S. J. Bame, R. C. Elphic, and C. T. Russell (1990), Plasma flow reversals at the dayside magnetopause and the origin of asymmetric polar cap connection, *J. Geophys. Res.*, *95*, 8073.

Haerendel, G., G. Paschmann, N. Sckopke, H. Rosenbauer, and P. C. Hedgecock (1978), The frontside boundary layer of the magnetosphere and the problem of reconnection, *J. Geophys. Res.*, *83*, 3195.

Harnett, E. M., and R. M. Winglee (2003), 3D fluid simulations of the Martian magnetosphere, *Geophys. Res. Lett.*, *30*(20), 2074, doi:10.1029/2003GL017852.

Harnett, E. M., and R. M. Winglee (2005), 3D multi-fluid simulations of Pluto's magnetosphere: A comparison to 3D hybrid simulations, *Geophys. Res. Lett.*, *32*, L19104, doi:10.1029/2005GL023178.

Harnett, E. M., and R. M. Winglee (2007), High-resolution multifluid simulations of the plasma environment near the Martian magnetic anomalies, *J. Geophys. Res.*, *112*, A05207, doi:10.1029/2006JA012001.

Harnett, E. M., R. M. Winglee, and P. Delamere (2005), 3D multi-fluid simulations of Pluto's magnetosphere: A comparison to 3D hybrid simulations, *Geophys. Res. Lett.*, *32*, L19104, doi:10.1029/2005GL023178.

Karimabadi, H., D. Krauss-Varban, J. D. Huba, and H. X. Vu (2004), On magnetic reconnection regimes and associated three-dimensional asymmetries: Hybrid Hall-less hybrid, and Hall-MHD simulations, *J. Geophys. Res.*, *109*, A09205, doi:10.1029/2004JA010478.

Lee, L. C., and Z. F. Fu (1986), Multiple X line reconnection. I. A criterion for the transition from a single X line to multiple X line reconnection, *J. Geophys. Res.*, *91*, 6807.

Ma, Z. W., and A. Bhattacharjee (1996), Fast impulsive reconnection and current sheet intensification due to electron pressure gradients in semi-collisional plasmas, *Geophys. Res. Lett.*, *23*, 1673.

Ogino, T. (1986), A three-dimensional MHD simulation of the interaction of the solar wind with the Earth's magnetosphere: the generation of field-aligned currents, *J. Geophys.*, *91*, 6791.

Paschmann, G. (1997), Observational evidence for transfer of plasma across the magnetopause, *Space Sci. Rev.*, *80*, 217.

Paty, C., and R. Winglee (2004), Multi-fluid simulations of Ganymede's magnetosphere, *Geophys. Res. Lett.*, *31*, L24806, doi:10.1029/2004GL021220.

Paty, C., and R. Winglee (2006), The role of ion cyclotron motion at Ganymede: Magnetic field morphology and magnetospheric dynamics, *Geophys. Res. Lett.*, *33*, L10106, doi:10.1029/2005GL025273.

Pritchett, P. L., F. V. Coroniti, and V. K. Decyk (1996), Three-dimensional stability of thin quasi-neutral current sheets, *J. Geophys. Res.*, *101*, 27,413.

Russell, C. T. (1989), The magnetopause, in *Physics of Magnetic Flux Ropes*, *Geophys. Monogr. Ser.*, vol. 58, edited by C. T. Russell, E. R. Priest, and L. C. Lee, p. 439, AGU, Washington, D. C.

Russell, C. T., and R. C. Elphic (1978), Initial ISEE magnetometer results: Magnetopause observations, *Space Sci. Rev.*, *22*, 681.

Shay, M. A., J. F. Drake, R. E. Denton, and D. Biskamp (1998), Structure of the dissipation region during collisionless magnetic reconnection, *J. Geophys. Res.*, *103*, 9165.

Shay, M. A., J. F. Drake, B. N. Rogers, and R. E. Denton (1999), The scaling of collisionless magnetic reconnection for large systems, *Geophys. Res. Lett.*, *26*, 2163.

Shay, M. A., J. F. Drake, and B. N. Rogers (2001), Alfvenic collisionless magnetic reconnection and the Hall term, *J. Geophys. Res.*, *106*, 3759.

Slinker, S. P., J. A. Fedder, and J. G. Lyon (1995), Plasmoid formation and evolution in a numerical simulation of a substorm, *J. Geophys. Res.*, *22*, 859.

Sonnerup, B. U. Ö., H. Hasegawa, and G. Paschmann (2004), Anatomy of a flux transfer event seen by Cluster, *Geophys. Res. Lett.*, *31*, L11803, doi:10.1029/2004GL020134.

Winglee, R. M. (1994), Non-MHD influences on the magnetospheric current system, *J. Geophys. Res.*, *99*, 13,437.

Winglee, R. M. (2000), Mapping of ionospheric outflows into the magnetosphere for varying IMF conditions, *J. Atmos. Sol. Terr. Phys.*, *62*, 527.

Winglee, R. M. (2004), Influence of heavy ion outflows on tail reconnection and the auroral current system, *J. Geophys. Res.*, *109*, A09206, doi:10.1029/2004JA010385.

Winglee, R. M., S. Kokubun, R. P. Lin, and R. P. Lepping (1998), Flux rope structures in the magnetotail: Comparison between Wind/Geotail observations and global simulations, *J. Geophys. Res.*, *103*, 135.

Winglee, R. M., D. Chua, M. Brittnacher, G. K. Parks, and G. Lu (2002), Global impact of ionospheric outflows on the dynamics of the magnetosphere and cross-polar cap potential, *J. Geophys. Res.*, *107*(A9), 1237, doi:10.1029/2001JA000214.

Winglee, R. M., W. Lewis, and G. Lu (2005), Mapping of the heavy ion outflows as seen by IMAGE and multi-fluid global modeling for the April 17, 2002 storm, *J. Geophys. Res.*, *110*, A12S24, doi:10.1029/2004JA010909.

Zhu, Z., and R. M. Winglee (1996), Tearing instability, flux ropes, and the kinetic current sheet kink instability in the Earth's magnetotail: A three-dimensional perspective from particle simulations, *J. Geophys. Res.*, *101*, 4885.

E. Harnett, J. Porter, A. Stickle, and R. M. Winglee, Department of Earth and Space Sciences, University of Washington, Seattle, WA 98195-1310, USA. (winglee@geophys.washington.edu)